A hybrid finite volume/finite element method for shallow water waves by static deformation on seabeds

Alia Al-Ghosoun* **Ashraf Osman†** **Mohammed Seaid‡**

Abstract

Unlike wind waves, water waves due to bed deformation are the result of the balance between bed stresses acting on the seabed of the ocean and the gravitational force trying to restore the equilibrium water surface. When these waves approach the coastline they begin to transform as they enter shallow water regime. As each wave begins to experience the seabed, both runup and overtopping occur. For example, recording ocean-bottom pressures in offshore regions has increased our understanding of tsunami sources and promoted the development of rapid source estimation for early tsunami warning. Numerical solutions of the water depth and velocity at the interface have an important impact on these efforts. Full understanding of the system requires resolution of not only the water depth but also the velocity in the sea-surface and the pressure at the sea-bottom. In the present study we develop a new coupled model for numerical simulations of wave runup by pre-defined static deformation on seabeds. The governing equations consist of the depth-averaged shallow water system including friction terms for the water free-surface coupled to the well-known second-order solid elastostatic formulation for the bed deformation. The model is fully coupled and at the interface between the water flow and the seabed, transfer conditions are implemented. Here, hydrostatic pressure and friction forces are considered for the elastostatic equations whereas bathymetric forces are accounted for in the shallow water equations. As numerical solvers, we propose a well-balanced finite volume method for the flow system and a stabilized finite element method for elastostatics. A special numerical treatment of wet/dry fronts in the proposed coupled system is also discussed in this study. We present numerical results for two test examples for wave runup by deformation on seabeds. In the current work, the effects of bed slope and the friction force on the flow field and free-surface waves are investigated in details.

Keywords. Shallow water equations; Linear elasticity; Finite volume method; Finite element method; Wave runup; Wet/dry treatment.

1 Introduction

Water waves generated by the deformation on seabeds are of general interest to coastal and ocean engineering. The study of bed deformations is of great complexity since it is a class of natural phenomena that occur under certain conditions such as earthquakes, water mass movement, storms and heavy rain falls, see [12, 15, 26] among others. In such events, bed deformations are capable of generating several types of long waves due to the energy transfer to the water volume. Free-surface waves generated by bed deformations include very powerful and destructive tsunami waves which propagate and can runup near offshore coastal areas and produce catastrophic waves causing significant coastal runup [8, 36]. In recent years, a considerable research effort has been developed regarding the mathematical modelling and numerical simulation of

*Department of Engineering, University of Durham, South Road, Durham DH1 3LE, UK *E-mail:* alia.r.al-ghosoun@durham.ac.uk

†Department of Engineering, University of Durham, South Road, Durham DH1 3LE, UK *E-mail:* ashraf.osman@durham.ac.uk

‡Department of Engineering, University of Durham, South Road, Durham DH1 3LE, UK *E-mail:* m.seaid@durham.ac.uk

the interaction between bed deformation and water waves as well as the mechanisms of the surface gravity wave generations and propagations. In general, the modelling of wave runup by static deformation is based on two components including the description of bed deformation and the governing equations of the water motion. Numerous investigations for the wave-induced by the deformations in seabeds have been carried out since the 1970s, see for example [38, 6, 16]. Numerical simulations also have been widely carried out to examine such a problem in recent years. Authors in [2] studied a buried pipeline in a region that is surrounded by two impermeable walls. Researchers in [20] have considered a similar case with a wider range of degree of saturation whereas, soil-pipeline contact effects and inertial forces in a new model have been investigated in [19]. In experimental investigations, the research contributions can be distinguished into two parts (i) field measurements and (ii) laboratory experiments. In the field measurement studies, data of pressure at the seabed surface and pore water pressure, vertical and horizontal total stresses in seabed have been collected, analyzed and compared with their theoretical counterparts in [22, 21, 35] among others. In laboratory experiment studies reported in [32], the pore pressure in seabed induced by progressive waves in wave flumes have been studied and compared with the results derived from linear wave theory. On the other hand, several numerical algorithms were proposed to accommodate complex geometry and physical conditions. For example, researchers in [9] have developed a simplified finite element model for isotropic and saturated permeable seabeds. In order to improve the computational efficiency, a radial point interpolation meshless method has been implemented in [33].

Shallow water equations have been typically used to model a wide variety of applications in free-surface flows and most of these applications involve wetting and drying over variable topography. Developing numerical techniques resolving wetting and drying fronts is becoming increasingly important in computational hydraulics. Predictions of flooding due to a breached dam, or overtopped levee are very crucial for disaster planning. Wave run-up estimates are needed for breach and coastal structure designs. Considerable numerical models have been developed for these problems and different techniques to solve the wetting and drying process have employed. Early models were initialized with a thin-layer of water everywhere in the domain [23]. To track the wet/dry boundaries, many finite element and finite difference models use a fixed computational grid to monitor the wetting and drying of grid nodes [28]. This approach may become computationally expensive and not sufficiently robust to simulate flow in arbitrary terrains as the grid must be readaptive at each time step for which computational nodes must be removed during recession or added during flooding to reduce grid distortion errors. A more robust and efficient method has been proposed in [11] in which the wet area of the computational mesh is fixed and gridpoints are added and subtracted at the wet/dry interfaces. However, all of the aforementioned methods use either finite differences or finite elements to discretize the shallow water equations. Finite element methods conserve mass over the entire domain, but not within each element or at each node. In general, most finite difference and finite element methods yield spurious oscillations at flow discontinuities unless a first-order accurate method or artificial viscosity are employed, see for instance [17] and further references are therein.

In the current study, a hybrid finite element/finite volume method for solving free-surface runup flow problems over deformable beds is proposed. Deformations in the topography can be generated by a localized force which causes propagations of the water waves with different amplitudes and frequencies. The governing equations consist of the nonlinear one-dimensional shallow water equations including friction terms for the water free-surface and the two-dimensional second-order solid elastostatic equations for the bed deformation. These equations are fully coupled and solved simultaneously in time using transfer conditions at the interface between the water flow and the seabed. This allow for hydrostatic pressure and friction forces to be implemented for the elastostatic equations whereas the deformed beds are accounted for in the shallow water equations through the bathymetric forces. As numerical solvers, we propose a well-balanced finite volume method for the shallow water system and a stabilized finite element method for linear elasticity equations. A new treatment of partially wet cells near the wet/dry boundaries is implemented in our finite volume/finite element method and a treatment for the bed friction near wet/dry boundaries is also implemented in the proposed approach. It should be pointed out that an inappropriate discretization of the bed friction terms over wet/dry boundaries in the computational domain could also be a source

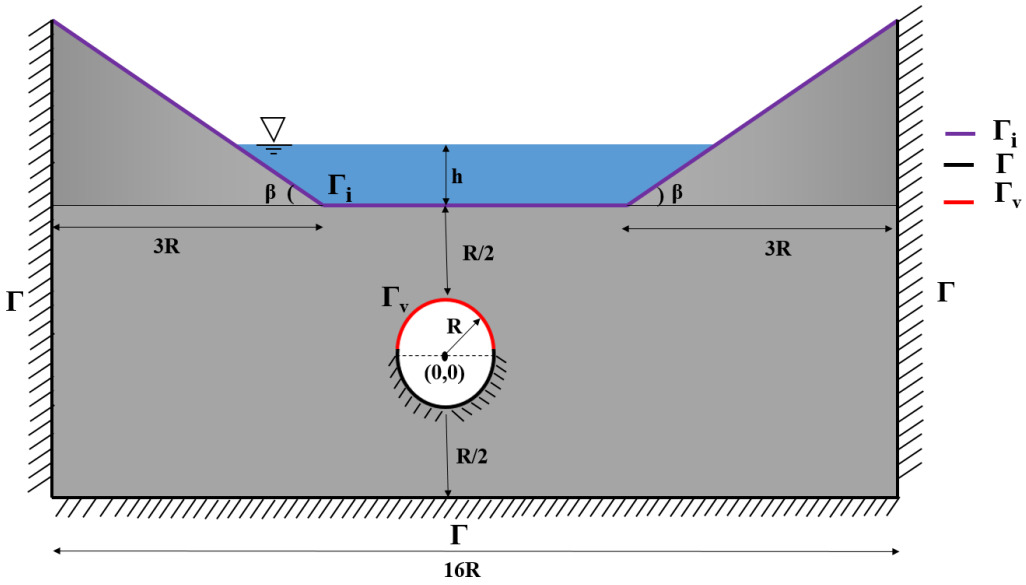

Figure 1.1: Schematic of a system for wave runup by elastic deformations in the topography. Here, the gray domain is used for the bed deformation and the blue domain is used for the water flow.

of nonphysical oscillations and numerical instabilities. This is mainly because in these regions, the water depth might be very small which yields incorrect predictions of the flow velocity that leads to unrealistically large errors in the predictions by the Manning's formula. Coupling conditions at the interface are also investigated in the current study, and the two-mesh procedure is proposed for the transfer of informations through the interface. The performance of the proposed finite volume/finite method is examined for two test examples for wave runup by deformation on seabeds due to a failure force applied in a circular void buried in the bed. The effects of bed slope and friction on the flow field and wave runup are investigated in this study. The paper is organized as follows: Description of the mathematical models for the coupled system is presented in section 2. Section 3 is devoted to the formulation of the numerical methods used for the solution procedure. Numerical results and examples for shallow water flows over elastic beds are presented in section 4. Concluding remarks are given in section 5.

2 Modelling wave runup by elastic deformations in the topography

For a two-dimensional homogeneous isotropic material domain $\Omega \subset R^2$ as shown in Figure 1.1, the equilibrium governing equations of linear elasticity read [30]

$$\begin{aligned} \frac{\partial \sigma_x}{\partial x} + \frac{\partial \tau_{xy}}{\partial y} &= f_x, \\ \frac{\partial \sigma_y}{\partial y} + \frac{\partial \tau_{xy}}{\partial x} &= f_y, \end{aligned} \tag{2.1}$$

where σ_x and σ_y are the normal stress components in the horizontal x-direction and the vertical y-direction, respectively. Here, τ_{xy} is the shear stress, f_x and f_y are the external forces in the x- and y-direction, respectively. The displacement vector is denoted by $\mathbf{u} = (u_x, u_y)^\top$ and the infinitesimal strain tensor is defined by

$$\boldsymbol{\epsilon} = \frac{1}{2}\Big(\nabla \mathbf{u} + (\nabla \mathbf{u})^\top\Big). \tag{2.2}$$

In the current study, we consider the constitutive relation

$$\boldsymbol{\sigma} = \mathbf{D}\,\boldsymbol{\epsilon}, \tag{2.3}$$

where the stress vector $\boldsymbol{\sigma}$ and the constitutive matrix $\mathbf{D}$ are defined by

$$\boldsymbol{\sigma} = \begin{pmatrix} \sigma_x \\ \sigma_y \\ \tau_{xy} \end{pmatrix}, \quad \mathbf{D} = \frac{E}{(1+\nu)(1-2\nu)} \begin{pmatrix} 1-\nu & \nu & 0 \\ \nu & 1-\nu & 0 \\ 0 & 0 & \dfrac{1-2\nu}{2} \end{pmatrix},$$

with ν is the Poisson ratio and E the Young modulus characterizing the bed material. Note that we solve the system (2.1) in the computational domain $\Omega \cup \Gamma \cup \Gamma_v \cup \Gamma_i$, with Ω is the interior domain, Γ the fixed boundary, Γ_v the forced boundary, and Γ_i the interface boundary between the bed topography and water body. In this case, the domain is a simple representation of a lake with two bed slopes at each end with angle β, and a pipe with given radius R is buried under the lake. The domain is subject to the following boundary conditions.

$$\begin{aligned} \mathbf{u} &= \mathbf{0}, \quad \text{on} \quad \Gamma, \\ \boldsymbol{\sigma} &= \boldsymbol{\sigma}_v, \quad \text{on} \quad \Gamma_v, \\ \sigma_y &= p, \quad \text{on} \quad \Gamma_i, \end{aligned} \tag{2.4}$$

where $\boldsymbol{\sigma}_v$ is a fixed stress on the boundary Γ_v and p is the hydrostatic pressure distribution at the interface Γ_i. Note that other boundary conditions for equations (2.1) can also be applied in the proposed finite volume/finite element method without major modifications in our formulation.

In the current work, as a consequence of bed deformations, a perturbation is expected to occur on the water surface. We also assume that no sediment transport is accounted for in this study. To solve for the water free-surface perturbations, a nonlinear shallow water system is considered. For one-dimensional problems, the shallow water equations are usually formulated in terms of surface elevation η and the water unit discharge q as [25]

$$\begin{aligned} \frac{\partial \eta}{\partial t} + \frac{\partial q}{\partial x} &= 0, \\ \frac{\partial q}{\partial t} + \frac{\partial}{\partial x}\left(\frac{q^2}{\eta - z} + \frac{g}{2}(\eta^2 - 2\eta z)\right) &= -g\eta\frac{\partial z}{\partial x} - \tau_f, \end{aligned} \tag{2.5}$$

where $\eta = h + z$, with $h(t,x)$ is the water depth and $z(x)$ the deformed bed. In (2.5), $q(t,x)$ is the unit width discharge given by $q = hv$, with $v(t,x)$ is the depth-averaged velocity and τ_f the bed friction force given as

$$\tau_f = g n_b^2 \frac{v\,|v|}{h^{\frac{1}{3}}}, \tag{2.6}$$

where g is the acceleration of gravity and n_b the Manning coefficient. For the numerical implementation, the shallow water system (2.5) can also be reformulated in term of h and hv as

$$\begin{aligned} \frac{\partial h}{\partial t} + \frac{\partial (hv)}{\partial x} &= 0, \\ \frac{\partial (hv)}{\partial t} + \frac{\partial}{\partial x}\left(hv^2 + \frac{1}{2}gh^2\right) &= -gh\frac{\partial z}{\partial x} - g n_b^2 \frac{v\,|v|}{h^{\frac{1}{3}}}, \end{aligned} \tag{2.7}$$

It should be noted that the coupled system (2.1)-(2.7) is numerically solved using a splitting operator where the bed deformation and the water free-surface are computed separately using the two-dimensional linear elasto-static equations (2.1) and the one-dimensional nonlinear shallow water equations (2.7). The coupling between the two models is achieved through the interface Γ_i by updating the bed topography $z(x)$ at each deformation step. Initially, the system is assumed at rest and a given external force $\mathbf{f} = (f_x, f_y)^\top$ is applied

on the boundary Γ_v at time $t = t_v$. The response of water free-surface to the deformation generated by the bed on Γ_i is examined using the shallow water system (2.1) with variable topography z. The effect of water on the bed is accounted for using the vertical force generated by the hydrostatic pressure and the horizontal force originated by the friction term as

$$p = -\rho g(h - \eta_0), \qquad \tau_f = -g n_b^2 \frac{v\,|v|}{h^{\frac{1}{3}}}, \qquad \text{on} \quad \Gamma_i \tag{2.8}$$

where ρ is the water density and $\eta_0 = h_0 + z$ with h_0 is the initial water depth. It is worth remarking that the interaction between the bed topography and the water free-surface depends on the properties of the soil forming the bed, the magnitude of the applied force, and the initial water depth among others. It should also be stressed that, in most engineering applications, the effect of changes in the water surface at each time step on the bed is assumed negligible compared to the effects of bed deformation on the water free-surface, compare [9] among others.

3 Hybrid finite volume/finite element method

To solve the coupled model for wave runup by static deformation on seabeds we consider a finite element method for the two-dimensional elasticity equations (2.1) and a finite volume method for the shallow water system (2.7). The starting point for the finite element method is the variational formulation of the strain energy in the domain Ω. Thus, multiplying the strong form of x-direction equation in (2.1) by a weight function ϕ_x and integrate over the domain yields

$$\int_\Omega \frac{\partial \sigma_x}{\partial x}\phi_x \, d\mathbf{x} + \int_\Omega \frac{\partial \tau_{xy}}{\partial y}\phi_x \, d\mathbf{x} - \int_\Omega f_x \phi_x \, d\mathbf{x} = 0.$$

Using the Green-Gauss theorem, the above equation becomes

$$\oint_{\partial\Omega} \sigma_x n_x \phi_x \, d\mathbf{x} - \int_\Omega \frac{\partial \phi_x}{\partial x}\sigma_x \, d\mathbf{x} + \oint_{\partial\Omega} \tau_{xy} n_y \phi_x \, d\mathbf{x} - \int_\Omega \frac{\partial \phi_x}{\partial y}\tau_{xy} \, d\mathbf{x} - \int_\Omega f_x \phi_x \, d\mathbf{x} = 0,$$

where $\mathbf{x} = (x, y)^\top$ and $\mathbf{n} = (n_x, n_y)^\top$ is the outward unit normal on Γ, $\partial\Omega = \Gamma \cup \Gamma_i \cup \Gamma_v$ Using the x-component of the traction $\mathcal{T}_x = \sigma_x n_x + \tau_{xy} n_y$, the above equation can be written as

$$\oint_{\partial\Omega} \mathcal{T}_x \phi_x \, d\mathbf{x} - \int_\Omega \left(\frac{\partial \phi_x}{\partial x}\sigma_x + \frac{\partial \phi_x}{\partial y}\tau_{xy} \right) \, d\mathbf{x} - \int_\Omega f_x \phi_x \, d\mathbf{x} = 0. \tag{3.1}$$

Similar steps applied to the y-direction equation in (2.1) give

$$\oint_{\partial\Omega} \mathcal{T}_y \phi_y \, d\mathbf{x} - \int_\Omega \left(\frac{\partial \phi_y}{\partial x}\tau_{xy} + \frac{\partial \phi_y}{\partial y}\sigma_y \right) \, d\mathbf{x} - \int_\Omega f_y \phi_y \, d\mathbf{x} = 0, \tag{3.2}$$

where $\mathcal{T}_y = \sigma_y n_y + \tau_{xy} n_x$. Adding the two equations (3.1) and (3.2) yields

$$\oint_{\partial\Omega} (\mathcal{T}_x \phi_x + \mathcal{T}_y \phi_y) \, d\mathbf{x} - \int_\Omega (f_x \phi_x + f_y \phi_y) \, d\mathbf{x} - \int_\Omega \left(\frac{\partial \phi_x}{\partial x}\sigma_x + \frac{\partial \phi_x}{\partial y}\tau_{xy} + \frac{\partial \phi_y}{\partial y}\sigma_y + \frac{\partial \phi_y}{\partial x}\tau_{xy} \right) \, d\mathbf{x} = 0,$$

which can be reformulated in a vector form as

$$\int_\Omega \widehat{\boldsymbol{\phi}} \cdot \boldsymbol{\sigma} \, d\mathbf{x} = \oint_{\partial\Omega} \boldsymbol{\phi}^\top \cdot \boldsymbol{\mathcal{T}} \, d\mathbf{x} + \int_\Omega \boldsymbol{\phi}^\top \cdot \mathbf{f} \, d\mathbf{x}, \tag{3.3}$$

where $\boldsymbol{\phi} = (\phi_x, \phi_y)^\top$, $\boldsymbol{\mathcal{T}} = (\mathcal{T}_x, \mathcal{T}_y)^\top$ and $\widehat{\boldsymbol{\phi}} = \left(\frac{\partial \phi_x}{\partial x}, \frac{\partial \phi_y}{\partial y}, \frac{\partial \phi_x}{\partial y} + \frac{\partial \phi_y}{\partial x} \right)^\top$. To solve the weak form (3.3) with the finite element method, the domain Ω is discretized into a set of elements where the solution is approximated in terms of the nodal values U_j and the polynomial basis functions $N_j(x, y)$ as

$$\mathbf{u}(x, y) = \sum_{j=1}^{N_d} \mathbf{U}_j N_j(x, y), \tag{3.4}$$

where N_d is the number of mesh nodes. In the present work, we consider quadratic triangular elements with six nodes for which the element displacement $\mathbf{u}^e = (u_x^e, u_y^e)^\top$ can be obtained by

$$\mathbf{u}^e = \begin{pmatrix} N_1^e & 0 & N_2^e & 0 & \dots & 0 \\ 0 & N_1^e & 0 & N_2^e & \dots & N_6^e \end{pmatrix} \begin{pmatrix} u_{x1} \\ u_{y1} \\ u_{x2} \\ u_{y2} \\ \vdots \\ u_{x6} \\ u_{y6} \end{pmatrix},$$

where N_j^e are the shape functions written in the local coordinates $(\xi_1, \xi_2)^\top$ as

$$\begin{aligned} N_1^e(\xi_1,\xi_2) &= \xi_2\,(2\xi_2 - 1)\,, & N_2^e(\xi_1,\xi_2) &= \xi_1\,(2\xi_1 - 1)\,, \\ N_3^e(\xi_1,\xi_2) &= (1-\xi_1-\xi_2)\,(1-2\xi_1-2\xi_2)\,, & N_4^e(\xi_1,\xi_2) &= 4\xi_2\xi_1, \\ N_5^e(\xi_1,\xi_2) &= 4\xi_1\,(1-\xi_2-\xi_1)\,, & N_6^e(\xi_1,\xi_2) &= 4\,(1-\xi_2-\xi_1)\,\xi_2. \end{aligned}$$

To solve the fully discretized problem, the elementary matrices are assembled into a global system of equations

$$\mathbf{K}\mathbf{u} = \mathbf{b}, \tag{3.5}$$

where $\mathbf{K}$ is the global stiffness matrix, $\mathbf{u}$ the nodal displacement vector and $\mathbf{b}$ the force vector. In our simulations, the linear system (3.5) of algebraic equations is solved using the conjugate gradient solver with incomplete Cholesky decomposition.

To solve the shallow water equations we consider a finite volume method of Godunov type. We reformulate the equations (2.7) in a conservative form as

$$\frac{\partial \mathbf{W}}{\partial t} + \frac{\partial \mathbf{F}(\mathbf{W})}{\partial x} = \mathbf{Q}(\mathbf{W}) + \mathbf{S}(\mathbf{W}), \tag{3.6}$$

where

$$\mathbf{W} = \begin{pmatrix} h \\ \\ hv \end{pmatrix}, \quad \mathbf{F}(\mathbf{W}) = \begin{pmatrix} hv \\ \\ hv^2 + \frac{1}{2}gh^2 \end{pmatrix}, \quad \mathbf{Q}(\mathbf{W}) = \begin{pmatrix} 0 \\ \\ -gh\dfrac{\partial z}{\partial x} \end{pmatrix}, \quad \mathbf{S}(\mathbf{W}) = \begin{pmatrix} 0 \\ \\ -gn_b^2\dfrac{v\,|v|}{h^{\frac{1}{3}}} \end{pmatrix}.$$

We also use the splitting operator introduced in [29] to deal with the differential source terms $\mathbf{Q}(\mathbf{W})$ and the non-partial derivative source term $\mathbf{S}(\mathbf{W})$ in (2.8). The splitting procedure consists of the following two steps:

Step 1: Solve for $\widetilde{\mathbf{W}}$

$$\frac{\widetilde{\mathbf{W}} - \mathbf{W}^n}{\Delta t} + \frac{\partial \mathbf{F}(\mathbf{W}^n)}{\partial x} = \mathbf{Q}\left(\mathbf{W}^n\right). \tag{3.7}$$

Step 2: Solve for $\mathbf{W}^{n+1}$

$$\frac{\mathbf{W}^{n+1} - \widetilde{\mathbf{W}}}{\Delta t} = \mathbf{S}\left(\widetilde{\mathbf{W}}\right). \tag{3.8}$$

For the space discretization of equation (3.6) we discretize the one-dimensional space domain in uniform cells $\left[x_{i-\frac{1}{2}}, x_{i+\frac{1}{2}}\right]$ with same length Δx for simplicity, we also divide the time interval into subintervals

$[t_n, t_{n+1}]$ with size Δt and $t_n = n\Delta t$. We also use the notation $\mathbf{W}_i(t)$ to denote the space-averaged of $\mathbf{W}(t,x)$ in the cell $\left[x_{i-\frac{1}{2}}, x_{i+\frac{1}{2}}\right]$ at time t, and $\mathbf{W}_{i+\frac{1}{2}}$ is the intermediate solution at $x_{i+\frac{1}{2}}$ at time t,

$$\mathbf{W}_i(t) = \frac{1}{\Delta x}\int_{x_{i-\frac{1}{2}}}^{x_{i+\frac{1}{2}}} \mathbf{W}(t,x)\, dx, \qquad \mathbf{W}_{i+\frac{1}{2}} = \mathbf{W}\left(t, x_{i+\frac{1}{2}}\right).$$

Integrating the system (3.7) over the time-space control domain $[t_n, t_{n+1}] \times \left[x_{i-\frac{1}{2}}, x_{i+\frac{1}{2}}\right]$, one obtains the following fully discrete system

$$\widetilde{\mathbf{W}}_i = \mathbf{W}_i^n - \frac{\Delta t}{\Delta x}\left(\mathbf{F}_{i+\frac{1}{2}}^n - \mathbf{F}_{i-\frac{1}{2}}^n\right) + \Delta t \mathbf{Q}_i^n, \tag{3.9}$$

where $\mathbf{F}_{i\pm\frac{1}{2}}^n = \mathbf{F}\left(\mathbf{W}_{i\pm\frac{1}{2}}^n\right)$ are the numerical fluxes at $x = x_{i\pm\frac{1}{2}}$ and time $t = t_n$, and $\mathbf{Q}_i^n$ is a consistent discretization of the source term $\mathbf{Q}$ in (3.7). The spatial discretization (3.9) is complete when the numerical fluxes $\mathbf{F}_{i\pm1/2}^n$ and the source term $\mathbf{Q}_i^n$ are reconstructed. Generally, this step can be carried out using any finite volume method developed in the literature for solving hyperbolic systems of conservation laws, see for example [2, 13]. In the present study, we consider the Roe reconstruction defined as [27]

$$\mathbf{F}_{i+\frac{1}{2}}^n = \frac{1}{2}\left(\mathbf{F}(\mathbf{W}_{i+1}^n) + \mathbf{F}(\mathbf{W}_i^n)\right) + \frac{1}{2}\mathbf{A}\left(\widehat{\mathbf{W}}_{i+\frac{1}{2}}^n\right)\left(\mathbf{W}_i^n - \mathbf{W}_{i+1}^n\right), \tag{3.10}$$

where the averaged state $\widehat{\mathbf{W}}_{i+\frac{1}{2}}^n$ is calculated as

$$\widehat{\mathbf{W}}_{i+\frac{1}{2}}^n = \begin{pmatrix} \dfrac{h_i^n + h_{i+1}^n}{2} \\ \\ \dfrac{\sqrt{h_i^n}v_i^n + \sqrt{h_{i+1}^n}v_{i+1}^n}{\sqrt{h_i^n + h_{i+1}^n}} \end{pmatrix},$$

and the Roe matrix in (3.10) is defined as $\mathbf{A} = \mathbf{R}\mathbf{L}\mathbf{R}^{-1}$ with

$$\mathbf{R} = \begin{pmatrix} 1 & 1 \\ \\ \widehat{\lambda}_1 & \widehat{\lambda}_2 \end{pmatrix}, \qquad \mathbf{L} = \begin{pmatrix} \widehat{\lambda}_1 & 0 \\ \\ 0 & \widehat{\lambda}_2 \end{pmatrix}, \tag{3.11}$$

with $\lambda_1 = v - \sqrt{gh}$ and $\lambda_2 = v + \sqrt{gh}$ are the two eigenvalues associated with the system. For the approximation of the source term in (3.9), we use the well-balanced discretization discussed in [3]. Hence, the discretization of the source term $\mathbf{Q}_i$ is carried out as

$$gh\frac{\partial z}{\partial x}\Big|_{x=x_i} \approx g\frac{h_{i+1} + 2h_i + h_{i-1}}{4}\frac{z_{i+1} - z_{i-1}}{2\triangle x}. \tag{3.12}$$

Note that, using this discretization of the source term, the scheme (3.9) satisfies the well-known C-property *i.e.*, for a stationary flow at rest

$$h^n + z = C, \qquad v^n = 0,$$

where C is a positive constant. Notice that other reconstructions such as HLL and HLLC methods [34, 37] can also be used for the numerical fluxes in (3.9).

It should be stressed that, dealing with wetting and drying problems, most of numerical methods for solving the shallow water equations (2.7) perturb the dry state using a defined threshold above which the solution state is considered to be dry. This is mainly used to avoid division by zero when updating

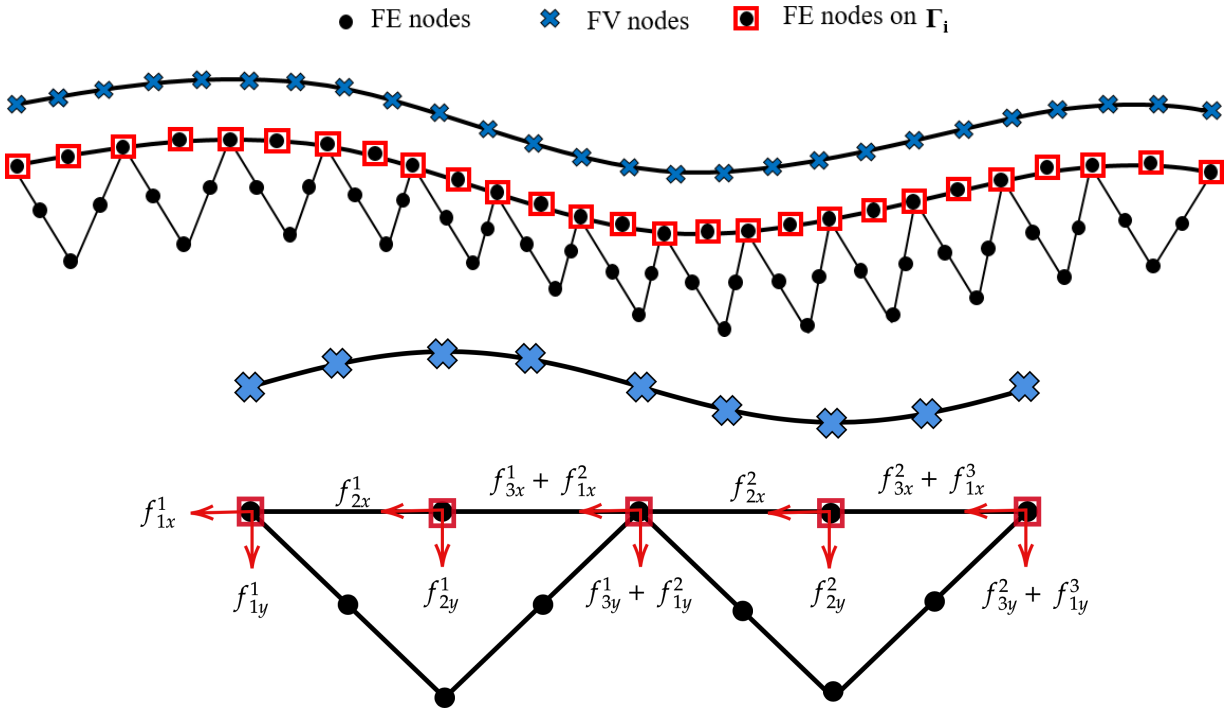

Figure 3.1: Illustration of finite element and finite volume nodes at the interface (top plot) and distribution of the horizontal and vertical forces on the finite element nodes (bottom plot).

the water velocity v during the simulation. Notice that, it is crucial to correctly solve this problem, as inaccurate results may lead to inaccuracy in the computed solutions or to false location of the wet/dry fronts in the runup zones, see [10, 4, 18] for more details. In the current work, we adapt the correction procedure proposed in [4] which is well-balanced even in the presence of dry areas. Here, at each time step the considered control volume $\left[x_{i-\frac{1}{2}}, x_{i+\frac{1}{2}}\right]$ is either a wet cell or a dry cell or a partially wet/dry cell. Thus, the wet/dry treatment is carried out as follows

$$h(t, x_i) = \begin{cases} h_i, & \text{if} \quad \eta_i \geq z_{max}, \\ \dfrac{1}{2}(h_i + z_i - z_{min}), & \text{if} \quad \eta_i > z_{min}, \\ z_{min} - z_i, & \text{if} \quad \eta_i \leq z_{min}, \\ 0, & \text{otherwise}, \end{cases} \tag{3.13}$$

where z_{min} and z_{max} are defined as

$$z_{min} = \min\left(z_i, z_{i+1}\right), \qquad z_{max} = \max\left(z_i, z_{i+1}\right).$$

In order to maintain a stable solution, a tolerance ε is defined and new velocities are computed in a fully wet cell only if $h_i^{n+1} > \varepsilon$. It should be noted that at dry cells, the source term $gh\frac{\partial z}{\partial x}$ is set to zero and at wet/dry fronts the treatment (3.13) is used for the approximation of water depth h in the discretization (3.12).

It is also evident that for small water depths, the bed friction term dominates the other terms in the momentum equation. This is mainly due to the presence of the term $h^{\frac{1}{3}}$ in the dominator of τ_f in (2.6).

To overcome this drawback we use a semi-implicit time integration of the source term $\mathbf{S}$ in (3.8) as

$$\begin{aligned} \frac{h^{n+1}-\widetilde{h}}{\Delta t} &= 0, \\ \frac{(hv)^{n+1}-\left(\widetilde{h}\widetilde{v}\right)}{\Delta t} &= -gn_b^2\frac{(hv)^{n+1}\,|\widetilde{v}|}{\left(\widetilde{h}\right)^{\frac{4}{3}}}, \end{aligned} \tag{3.14}$$

where $\widetilde{h}$ and $\widetilde{v}$ are the water depth and velocity obtained from the first step (3.7) of the splitting procedure. Solving the second equation in (3.14) for $(hv)^{n+1}$ yields

$$(hv)^{n+1} = \frac{\left(\widetilde{h}\widetilde{v}\right)}{1+\Delta t g n_b^2\dfrac{|\widetilde{v}|}{\left(\widetilde{h}\right)^{\frac{4}{3}}}}. \tag{3.15}$$

In general, the finite element and finite volume nodes on the interface do not coincide and therefore we use a cubic interpolation procedure to interchange the information between the two sets of nodes. As illustrated in Figure 3.1, at each time step coupling conditions occur at the interface for both models. In the present work, the deformed finite element nodes on the interface are used to reconstruct the bed z for the shallow water equations (2.7). This bed profile is used in the finite volume solution of the flow system to obtain the water depth h^{n+1} and the water velocity v^{n+1}. On the interface, the horizontal x-direction force f_x in the elasticity equations (2.1) is updated as

$$f_x = -gn_b^2\frac{v^{n+1}\left|v^{n+1}\right|}{(h^{n+1})^{\frac{1}{3}}}. \tag{3.16}$$

The vertical y-direction force f_y is reconstructed at each time step using the change in the hydrostatic pressure in (2.8) as

$$p^{n+1} = -\rho g(h^{n+1}-\eta_0),$$

and at each node of the three finite element nodes located on the interface, the force f_y is distributed using the integral form as

$$f_y^{(1)} = \int_{-1}^{1}\frac{1}{2}\xi\,(\xi-1)\,p^{n+1}\frac{\hbar}{2}\,d\xi = \frac{1}{6}p^{n+1}\hbar, \qquad f_y^{(2)} = \frac{2}{3}p^{n+1}\hbar, \qquad f_y^{(3)} = \frac{1}{6}p^{n+1}\hbar, \tag{3.17}$$

where $\hbar$ is the edge length of the considered element on interface. The total y-direction force f_y is obtained by accumulating the elemental forces on the overlapping nodes, see Figure 3.1 for an illustration. Note that both horizontal force f_x and vertical force f_y have negative signs and therefore are applied in the negative x- and y-direction, respectively. In summary, the finite volume/finite element method proposed in this study to solve wave runup by static deformation on seabeds is carried out in the steps described in Algorithm 1.

4 Numerical results

Test examples are presented in this section to illustrate the numerical performance of the techniques described above and verify numerically their capability to solve moving wet/dry fronts in shallow water flows. In the computations reported in this paper, the Courant number is set to $C_r = 0.75$ and the time stepsize Δt is adjusted at each time step according to the Courant-Friedrichs-Lewy (CFL) stability condition as

$$\Delta t = Cr\frac{\Delta x}{\max\left(|\lambda_1|\,,|\lambda_2|\right)}, \tag{4.1}$$

Algorithm 1 Finite volume/finite element method used in the present study.

Require: T the final time for the simulation.

Assemble the stiffness matrix $\mathbf{K}$ for elastostatic system using the finite element method (3.1)-(3.5).
while $t_{n+1} \leqslant T$ **do**
  Assemble the force vector $\mathbf{b}$ for elastostatic system using the finite element method (3.1)-(3.5).
  Solve the linear system (3.5) for the displacement in the computational mesh.
  Update the displacement of the finite element nodes on the interface.
  Reconstruct the bed z using a cubic interpolation from finite element nodes to finite volume cells.
  Adjust the time step Δt according to the CFL condition (4.1).
  Solve the shallow water equations using:
  for each control volume $\left[x_i, x_{i+\frac{1}{2}}\right]$ **do**
    Compute the numerical fluxes $\mathbf{F}^n_{i+\frac{1}{2}}$ using the Roe scheme (3.10).
    Discretize the source term $\mathbf{Q}_i$ using the well-balanced discretization (3.12).
    Compute the solution in the first stage of the splitting $\mathbf{W}_i^{n+1}$ using (3.9).
    Update the solution in the second stage of the splitting (3.8) using (3.14)-(3.15).
    Perform the wet/dry treatment according to (3.13) as:
    Evaluate $z_{min} = \min(z_i, z_{i+1})$ and $z_{max} = \max(z_i, z_{i+1})$ and check:
    if $\eta_i^{n+1} \geq z_{max}$ **then**
      $h = h_i^{n+1}$
    else if $\eta_i^{n+1} > z_{min}$ **then**
      $h = \frac{1}{2}(h_i^{n+1} + z_i - z_{min})$
    else if $\eta_i^{n+1} \leq z_{min}$ **then**
      $h = z_{min} - z_i$
    else
      $h = 0$
    end if
  end for
  Compute the horizontal force f_x using the bed friction according to (3.16).
  Compute the vertical force f_y using the hydrostatic pressure according to (3.17).
  Interpolate the forces f_x and f_y from finite volume cells to finite element nodes on the interface.
end while

where λ_1 and λ_2 are the two eigenvalues of the shallow water equations defined in (3.11). Notice that at each time step, the bed deformation leads to a change in the water depth and flow velocity which consequently affects the calculation of the eigenvalues (3.11). Hence, the effect of bed deformation is implicitly accounted for in updating the time step which involves in its variation the water depth and the flow velocity resulting from this deformation. We present numerical results for both, bed deformation and water free-surface at different times. In all simulations presented in this section and unless stated otherwise, the water density $\rho = 1000\ kg/m^3$, the gravitational acceleration $g = 9.81\ m/s^2$, the Young's modulus $E = 10000\ MPa$, the Poison's ratio $\nu = 0.3$, the tolerance $\varepsilon = 10^{-13}$ and the Manning coefficient $n_b = 0.05\ s/m^{1/3}$.

4.1 Validation of wet/dry treatment for dam-break problems

First we examine the procedure used in our approach for the wet/dry treatment in the finite volume method. To this end we consider the well-established experimental benchmark of dam-break over a dry bed studied in [14] among others. The importance of this test case comes from the fact that its solution includes most challenging flow features which many finite volume methods fail to capture. For example, wave reflections, repeatedly wetting and drying, presence of the surface curvatures, and non-differentiability topography are among these difficulties. Figure 4.1 illustrates the configuration of the domain and the initial conditions

Point	x (m)	y(m)
P_1	0.00	0.000
P_2	2.00	0.000
P_3	2.20	0.108
P_4	2.25	0.108
P_5	2.30	0.108
P_6	2.50	0.000
P_7	6.10	0.000
P_8	6.50	0.213
P_9	6.60	0.213
P_{10}	7.00	0.000

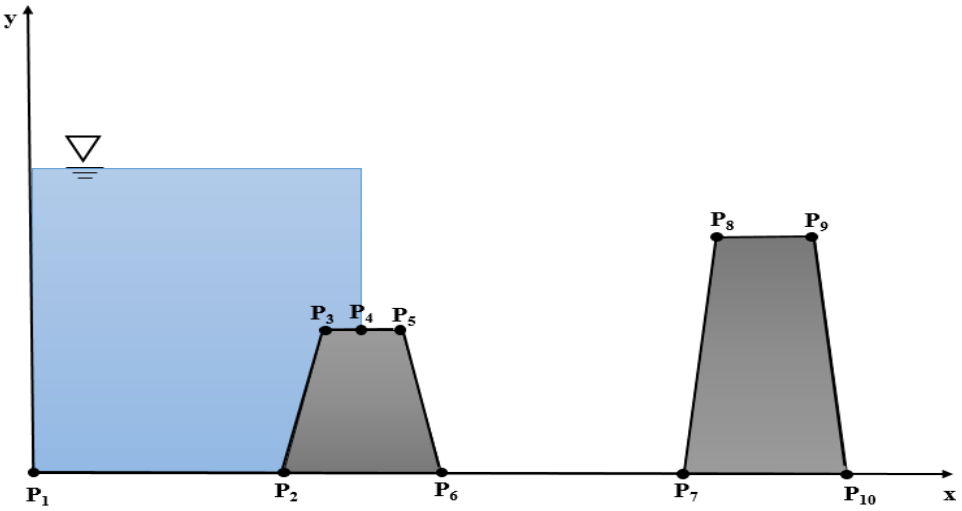

Figure 4.1: Illustration of the test example used for validation of the wet/dry treatment.

used in the simulations. Here, a dam-break problem over a dry bed with two humps is simulated in a 7 m long channel. The dam is located on the top of the first hump with a water depth of 0.342 m. The simulation is carried out for a total time of 15 s and the water depth is monitored at the channel downstream in the locations $x = 1.4\ m$, $x = 2.25\ m$ and $x = 4.5\ m$.

In Figure 4.2 we display the time evolution of the water depth obtained at $x = 1.4\ m$, $x = 2.25\ m$ and $x = 4.5\ m$ using our finite volume method compared to the experimental results. The domain is uniformly discretized into 144 control volumes in our simulations. As can be seen from the results in Figure 4.2, the finite volume method accurately captures the hydraulic jump and it resolves very well this free-surface flow over dry areas. However, the arrival of the second reflective wave at $x = 2.25\ m$ and $x = 4.50\ m$ are less accurately predicted by the numerical model. This may be attributed to the presence of three-dimensional flow structures at these locations for which the considered one-dimensional equations fail to capture correctly. There is a good agreement between the experimental and the numerical results for this test example at all considered locations. Therefore, one may conclude that the wet/dry treatment performs well for dam-break problems over dry beds and it resolves all the flow features without the need for refined meshes. Note that the performance of the considered finite volume method is very attractive since the computed flow solutions remain stable and highly accurate even coarse meshes are used without solving nonlinear problems or requiring special wet/dry correction procedures.

Next we compare the performance of the proposed wet/dry treatment to the conventional procedure which consists of perturbing the dry state using a wetted threshold above which the solution is considered to be dry. To this end we consider a dam-break problem in a frictionless flat rectangular channel ($z(x) = 0$) with known analytical solution. The channel is of 300 m length and the initial conditions are defined by

$$h(0,x) = \begin{cases} h_0, & \text{if} \quad x \leq x_0, \\ \\ 0, & \text{if} \quad x > x_0, \end{cases} \qquad\qquad v(0,x) = 0, \tag{4.2}$$

where $x_0 = 150\ m$ is the initial location of the wet/dry interface and $h_0 = 10\ m$ is the initial water depth. Here, the conventional approach uses a threshold of $\varepsilon = 10^{-13}$ and it is mainly used to avoid division by zero in updating the flow velocity during the simulation process. The analytical solution of this problem is

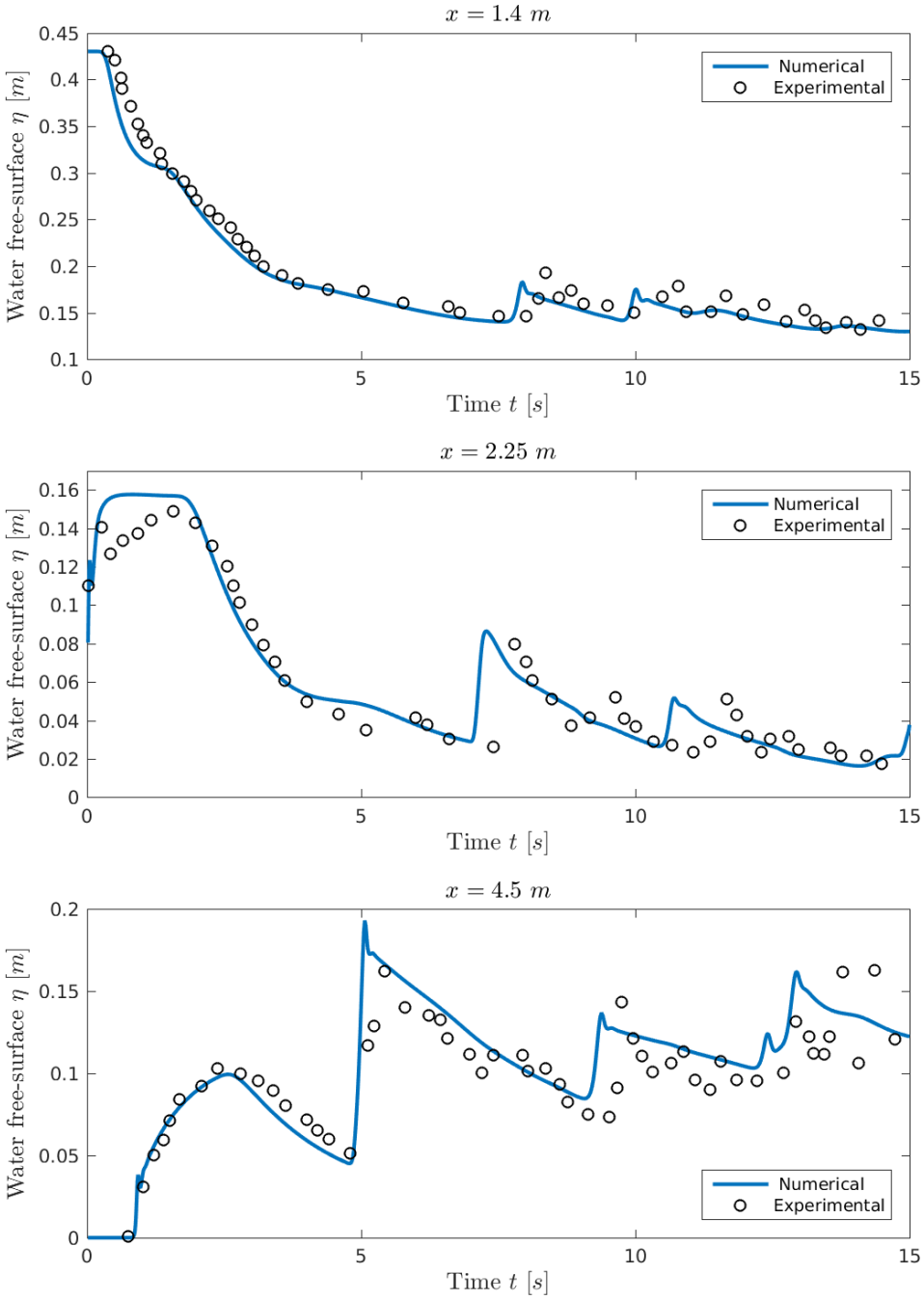

Figure 4.2: Comparison between experimental and numerical results for the dam-break problem over a non-flat dry bed at three different locations $x = 1.4\ m$, $x = 2.25\ m$ and $x = 4.5\ m$.

defined by [7]

$$h(t,x) = \begin{cases} h_0, & \text{if} \quad x \leq -t\sqrt{gh_0}, \\ \dfrac{1}{9g}\left(2\sqrt{gh_0} - \dfrac{x}{t}\right)^2, & \text{if} \quad -t\sqrt{gh_0} < x \leq 2t\sqrt{gh_0}, \\ 0, & \text{if} \quad x > 2t\sqrt{gh_0}, \end{cases}$$

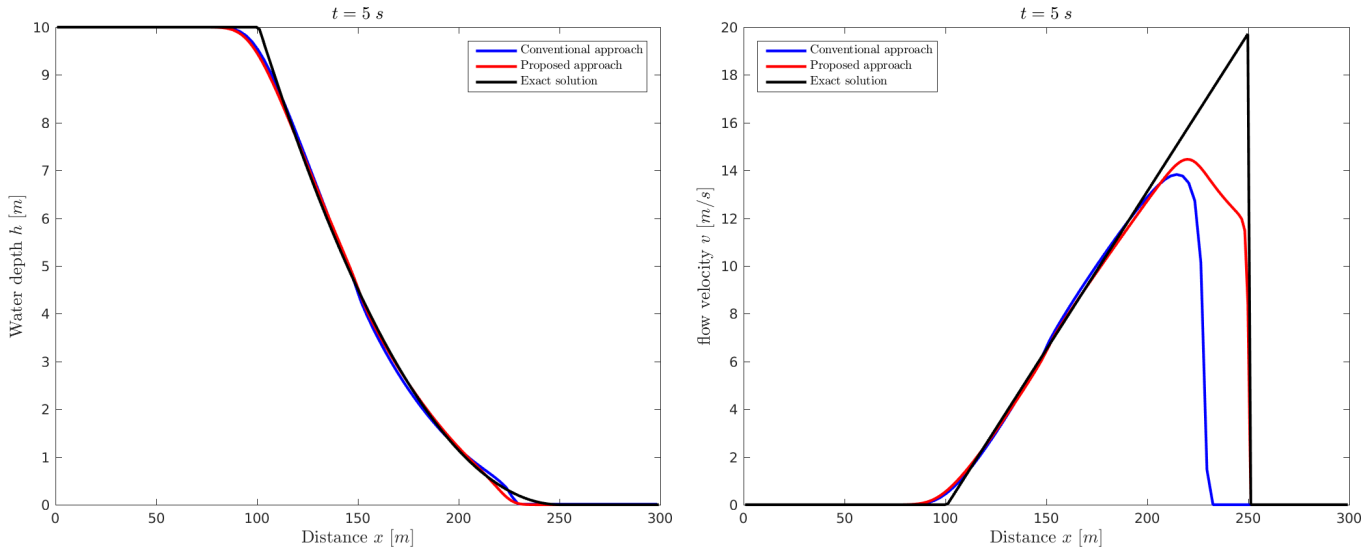

Figure 4.3: Comparison between the conventional approach and the proposed method for the wet/dry treatment in the dam-break problem over a dry bed with known analytical solution.

$$v(t,x) = \begin{cases} 0, & \text{if} \quad x \leq -t\sqrt{gh_0}, \\ \dfrac{2}{3}\left(\sqrt{gh_0} + \dfrac{x}{t}\right)^2, & \text{if} \quad -t\sqrt{gh_0} < x \leq 2t\sqrt{gh_0}, \\ 0, & \text{if} \quad x > 2t\sqrt{gh_0}. \end{cases}$$

In our simulations, we use 100 control volumes and results for water depth and velocity are presented at time $t = 5\ s$. Figure 4.3 depicts a comparison between the results obtained for the water depth and velocity using the conventional approach and the proposed wet/dry treatment. Both approaches correctly capture solutions of the water depth with the proposed approach slightly more accurate than the conventional approach. It is clear that the proposed partial wet/dry treatment is more accurate in updating the flow velocity than the conventional approach. In addition, perturbing the water depth may result in inaccuracy in the computed solutions and may lead to false or inaccurate location of the wet/dry fronts on the coastal zones.

To further compare the performance of the proposed wet/dry treatment to the conventional procedure, we consider the dam-break problem over a frictionless dry inclined plane investigated in [31, 1] among others. The computational domain is the interval $[-15, 15]$ discretized into 100 control volumes. Here, the bed function is defined by $z(x) = x\tan(\alpha)$, with α is the bed inclination angle set in our simulation to $\alpha = \frac{\pi}{60}$. Initially,

$$h(0,x) = \begin{cases} 1 - z(x), & \text{if} \quad x \leq 0, \\ 0, & \text{if} \quad x > 0, \end{cases} \qquad v(0,x) = 0. \tag{4.3}$$

In Figure 4.4 we display the time evolution of the wet/dry interface obtained using the conventional approach and the proposed wet/dry treatment along with the exact profile of the interface. Note that the analytical wet/dry front position is given as

$$\chi(t) = 2t\sqrt{g\cos(\alpha)} - 0.5gt^2\tan(\alpha).$$

It is clear that there is a good agreement between the analytical results and those obtained using the proposed wet/dry treatment. The conventional approach fails to accurately capture the correct wet/dry

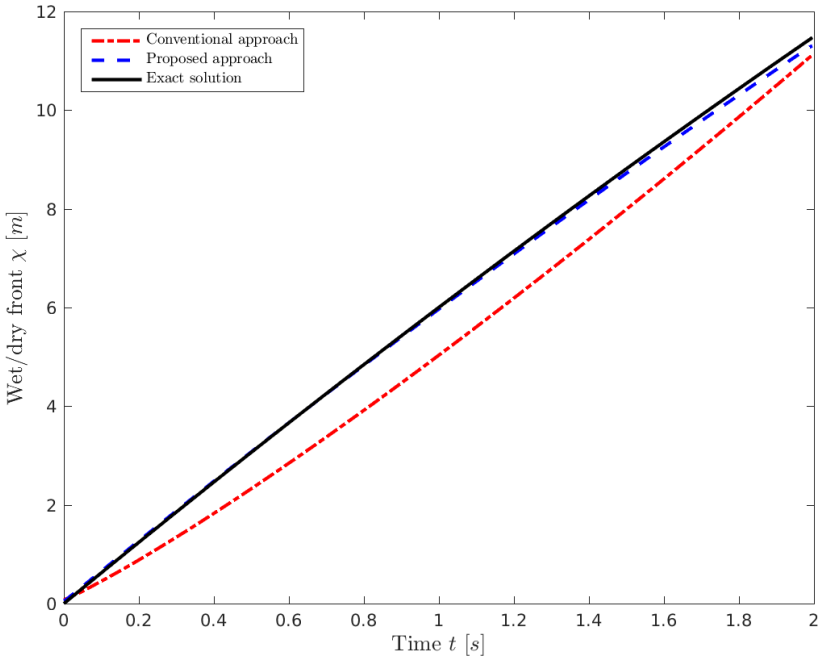

Figure 4.4: Comparison between the conventional approach and the proposed method for the wet/dry treatment in the dam-break problem over a dry inclined plane bed with known analytical wet/dry interface.

interface for this dam-break problem over non-flat dry beds. Again, the results in Figure 4.4 demonstrate the accuracy of the proposed technique in better resolving the moving wet/dry fronts than the conventional method.

We also validate the proposed approach for a dam-break problem over a wet bed against experimental measurements reported in [5]. As described in this reference, a glass channel with 9 m in length, 0.3 m in width and 0.34 m in height is used for the physical experiment. The dam is located at 4.65 m and the upstream water depth is fixed at $h_0 = 0.25$ m, whereas two values are used for the downstream water depth h_1. In this experiment, the dam-break is produced by lifting the gate upward very quickly through a pulley system. At time $t = 0$ the dam collapses and the flow problem consists of a shock wave traveling downstream and a rarefaction wave traveling upstream. We examine the performance of the proposed approach using 100 control volumes for $h_1 = 0.05$ m and $h_1 = 0.1$ m. In Figure 4.5 we present results obtained at dimensionless time $t = 6.51$. Note that dimensionless variables are used to display the results for which the distance x, time t and water depth h are divided by h_0, $\sqrt{\frac{h_0}{g}}$ and h_0, respectively. The agreement between the numerical simulations and experimental measurements in Figure 4.5 is fairly good. The free-surface amplitude and the hydraulic shock are well predicted by the proposed numerical approach. Obviously, the computed results for both considered values of h_1 verify the stability and the shock capturing properties of the numerical method for this dam-break problem over a wet bed.

4.2 Validation of finite element method for bed deformation

To verify the finite element method for solving two-dimensional elasticity equations, we consider the benchmark problem proposed in [24]. This problem has an analytical solution and it has been widely used in the literature to validate computational methods for elastostatic models. The problem statement consists on solving the equations (2.1) in a homogeneous and isotropic rectangular domain with 100 m for the length and 10 m for the width. The domain is subject to a nodal displacement of 3 m applied upwards in the center point of the domain. Here, the computational domain is discretized using quadratic finite elements in an unstructured triangular mesh with 772 elements and 1649 nodes. In Figure 4.6 we illustrate the mesh

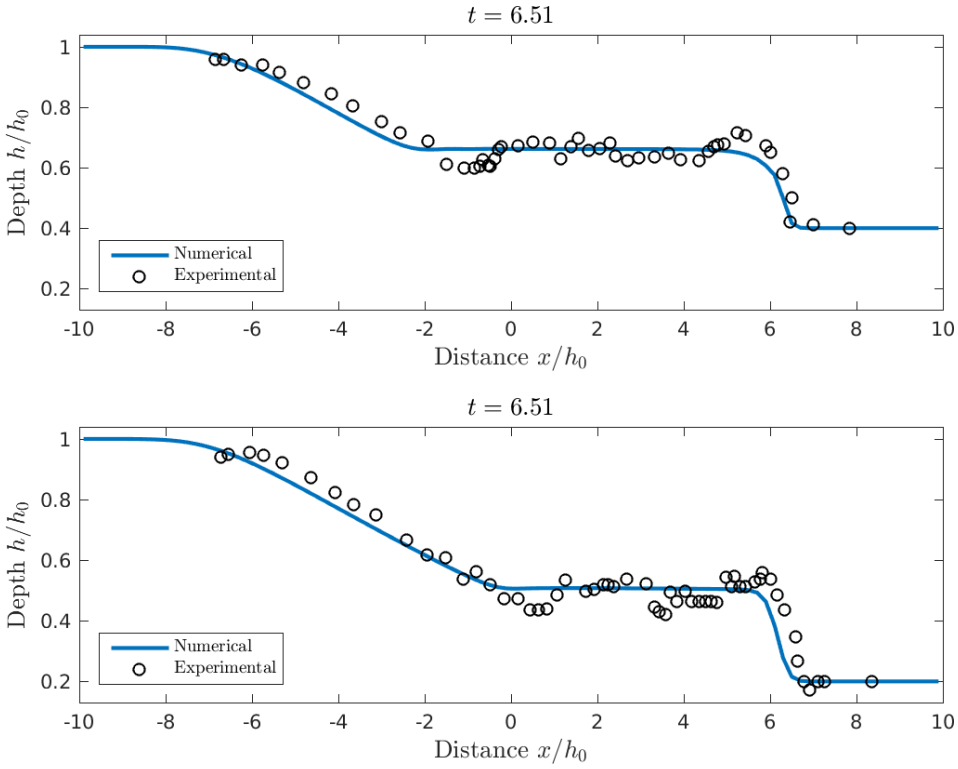

Figure 4.5: Comparison between experimental and numerical results for the dam-break problem over a wet bed at two different downstream water depths $h_1 = 0.1\ m$ and $h_1 = 0.05\ m$.

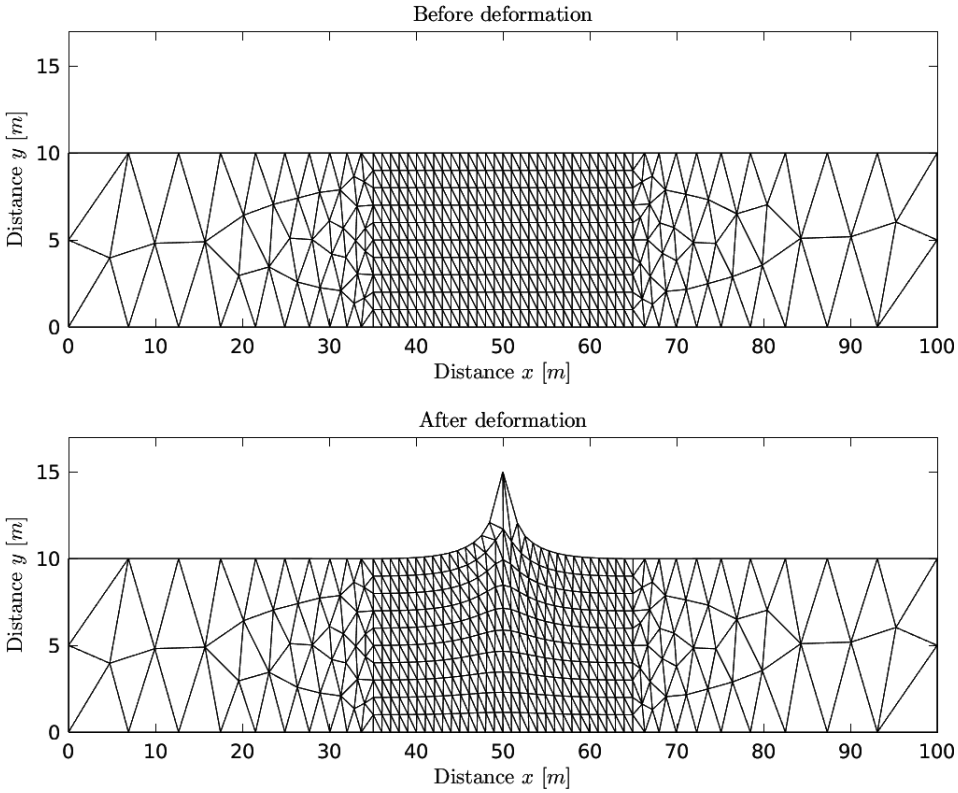

Figure 4.6: Computational mesh before deformation (top) and after deformation (bottom) used for the accuracy test example.

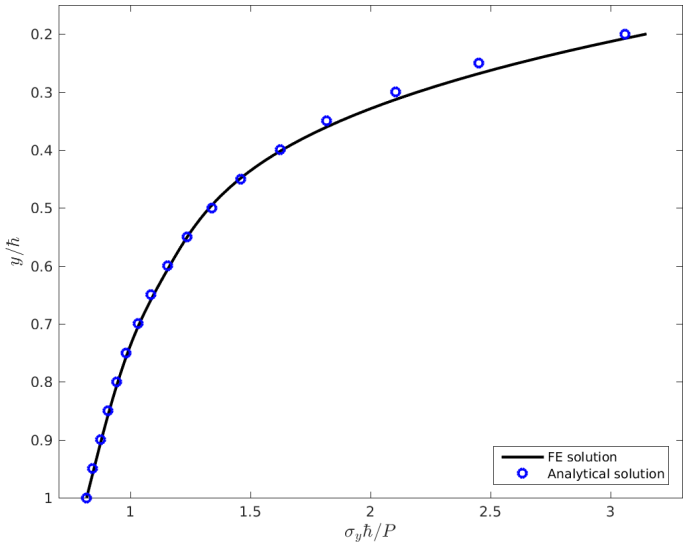

Figure 4.7: Comparison between the finite element results and the analytical solution of the vertical stress component σ_y for the accuracy test example.

used in our simulations before and after deformation by the nodal displacement. Note a denser mesh is used in our simulations for the area where the deformation is taken place. The comparison between the numerical results and analytical solution obtained for cross-sections of the vertical stress σ_y at the center point is presented in Figure 4.7. Notice that as discussed in [24], dimensionless variables are presented in Figure 4.7 using the domain width $\hbar = 10\ m$ and the point load $P = 3\ N/m$. As it can be seen from the results shown in Figure 4.6, the finite element method performs very well for this benchmark problem and it produces highly accurate and stable numerical results using reasonably coarse meshes. There is a good agreement between the results obtained using the finite element method and the analytical solution reported in [24].

4.3 Free-surface flow problem over a deformable bed

Pipe failures are among common examples in nature for which several studies have taken place in civil engineering. For these applications, the source of deformation may be caused by a fatigue in the pipe or simply by a load applied below the seabed. In this example, we consider a free-surface flow over a lake with runup slopes at both sides with open out-flow conditions at the downstream boundary and including a circular pipe as shown in Figure 1.1. Here, the pipe radius $R = 3\ m$ with a force of 100 N applied on the top surface of the pipe Γ_v, two values of the bed slope angle are considered in this section with $\beta = \frac{\pi}{5}$ and $\beta = \frac{\pi}{10}$. Initially, the system is at rest and to maintain the same water volume in the two cases, the water depth at time $t = 0$ is $h = 2.5\ m$ and $h = 2.1\ m$ for $\beta = \frac{\pi}{5}$ and $\beta = \frac{\pi}{10}$, respectively. Keeping the water volume the same in both cases and changing the bed slope angles would allow for a comparison in terms of the maximum water depth and the settling time for the waves in the considered situations. At time $t = 10\ s$ the constant force is applied on the upper part Γ_v of the pipe and consequently a deformation is expected on the pipe and therefore on the lake bed which generate water waves on the surface to runup over both slopes.

Figure 4.8 depicts the mesh used in our simulations before and after deformation for $\beta = \frac{\pi}{5}$. Based on a mesh convergence study not reported here for brevity, an unstructured triangular mesh with 1749 quadratic elements and 3763 nodes is used in our simulations as it offers a compromise between accuracy and efficiency in the numerical method. In Figure 4.9 we present the distribution of the main stress component σ_x at time $t = 12\ s$ for the considered bed slope angles $\beta = \frac{\pi}{5}$ and $\beta = \frac{\pi}{10}$. It is clear that maximum values of stresses

Table 4.1: Statistics for the hydraulic energy for free-surface flow problem over a deformable bed using different Manning coefficients.

	$\beta = \frac{\pi}{5}$					
n_b	min	Peak	Mean	Std	Rise time	Settling time
0.01	4.501	6.81	6.385	0.255	0.208	1.472×10^4
0.05	4.501	6.67	6.381	0.228	0.166	1.467×10^4
0.1	4.501	6.61	6.375	0.198	0.140	1.456×10^4

	$\beta = \frac{\pi}{10}$					
n_b	min	Peak	Mean	Std	Rise time	Settling time
0.01	4.901	7.206	6.742	0.269	0.154	1.559×10^4
0.05	4.901	7.103	6.746	0.257	0.144	1.558×10^4
0.1	7.901	7.016	6.741	0.234	0.126	1.555×10^4

are located on the pipe surface where the deformation has taken place. The deformed bed has also been accurately resolved using our finite element method. Under the considered conditions, stress distributions for both bed slopes exhibit similar features in the computational domain. Note the symmetrical features in both stress distributions and the bed profile in the obtained results in Figure 4.9. Furthermore, no mesh distortion has been detected in all results obtained for this test example. It should be stressed that results from the proposed coupled model should be compared with observations of laboratory free-surface flows and bed deformations for this problem. However, there is no data available until now to carry out this comparison study. Thus, at the moment we can only perform numerical simulations and verify that results are plausible and consistent.

In Figure 4.10 we display the responses of the water free-surface at five different instants for $\beta = \frac{\pi}{5}$. Those results obtained for $\beta = \frac{\pi}{10}$ are shown in Figure 4.11. We used a mesh with 100 control volumes for the solution of shallow water equations. As can be seen from these results, the system starts from the rest and once the deformation on the pipe occurs, a water wave is generated on the surface and it flows over the deformed bed. Later the water wave reaches the two bed slopes and a runup can be clearly seen in both bed slopes in Figure 4.10 and Figure 4.11. For longer times, the system is stabilized to a steady-state configuration with no disturbances on the water surface for both cases. A longer runup waves have been observed for the case with $\beta = \frac{\pi}{10}$ than for the case $\beta = \frac{\pi}{5}$. It is clear that the considered hybrid finite volume/finite element method performs well for this free-surface flow problem over a deformable bed as both the bed topography and the water free-surface are accurately captured without non-physical oscillations or excessive numerical diffusion appearing in the the numerical solutions. To assess the accuracy of the coupled model in dealing with moving boundaries of the run-up problem, Figure 4.12 illustrates the time evolution of water free-surface and the flow velocity at three different gauges in $x = -10$, 0 and 10. As expected, because of the symmetry in this problem, the water depths at the locations $x = -10$ and $x = 10$ are identical and high water depths are expected at the gauge situated at the center $x = 0$ where the deformation takes place. It is also clear that the flow velocities at the two gauges in $x = -10$ and $x = 10$ have the same amplitudes and opposite signs. As time progresses, amplitudes of both the flow velocity and the water free-surface decrease at all considered gauges. The proposed coupled model performs very well for this example and captures the correct run-up features without requiring complicated techniques or three-dimensional representations for the free-surface flows over deformable beds.

To examine the effects of friction on the water free-surface, we illustrate in Figure 4.13 the time evolution of the hydraulic energy at the center of the domain ($x = 0$) using different values of the Manning coefficient n_b for $\beta = \frac{\pi}{5}$ and $\beta = \frac{\pi}{10}$. It is evident that increasing the Manning coefficient results in a decrease in the hydraulic energy. This energy dissipation is expected in the system for high frictions on the bed. In

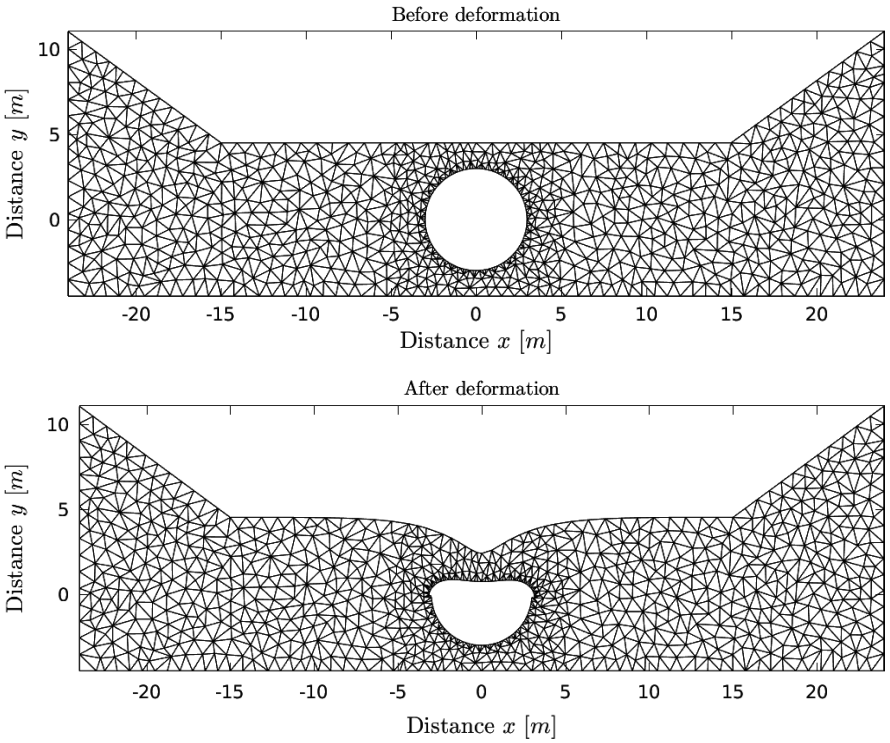

Figure 4.8: Computational mesh before deformation (top) and after deformation (bottom) used for free-surface flow problem over a deformable bed.

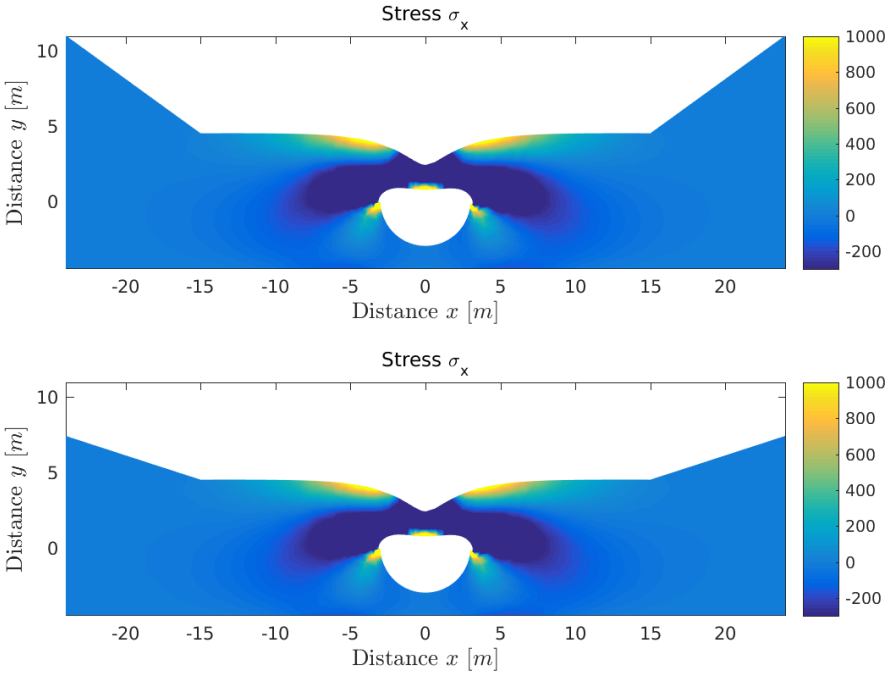

Figure 4.9: Distribution of the stress σ_x using $\beta = \frac{\pi}{5}$ (top) and $\beta = \frac{\pi}{10}$ (bottom) obtained for free-surface flow problem over a deformable bed at time $t = 12\ s$.

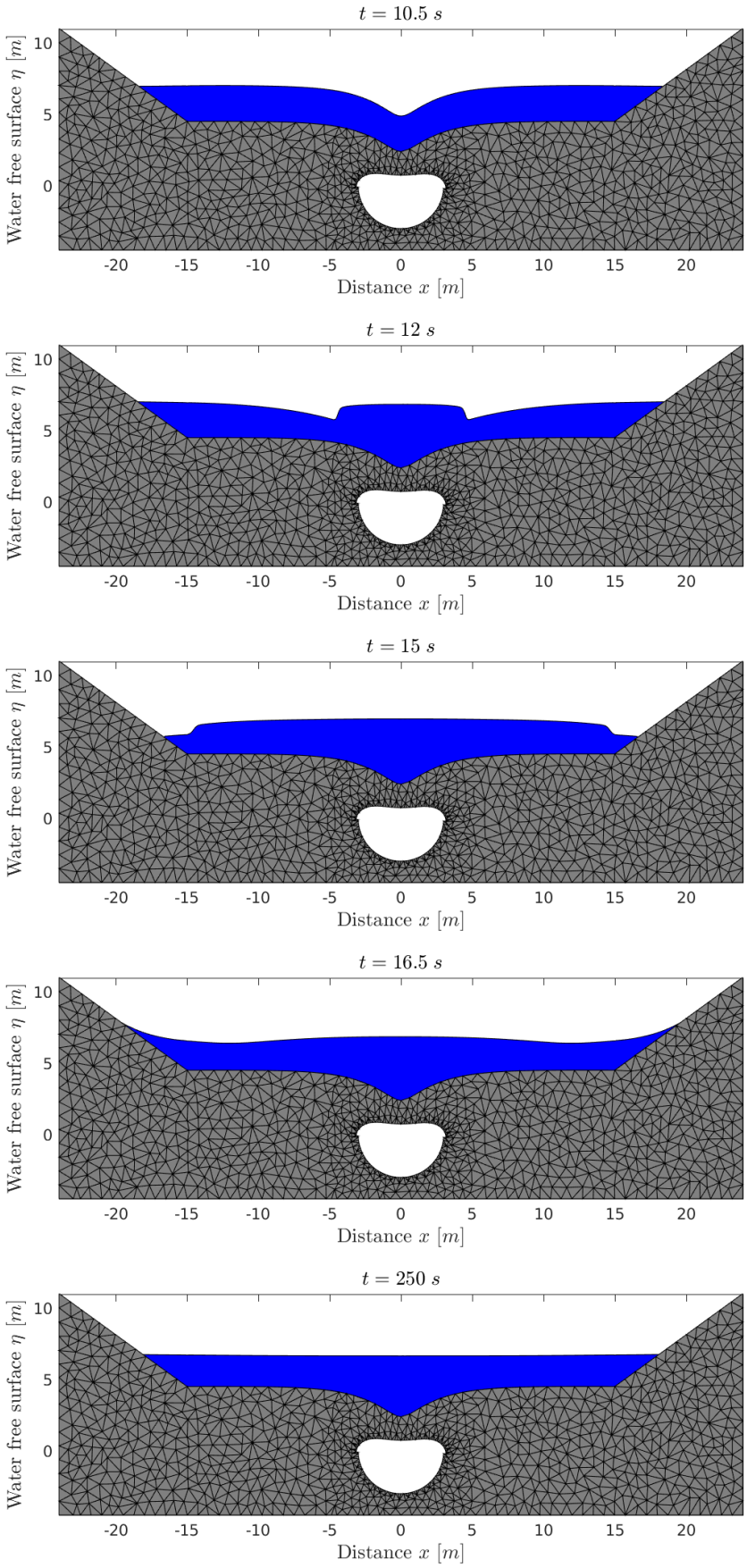

Figure 4.10: Free-surface responses at five different instants obtained for the flow problem over a deformable bed with $\beta = \frac{\pi}{5}$.

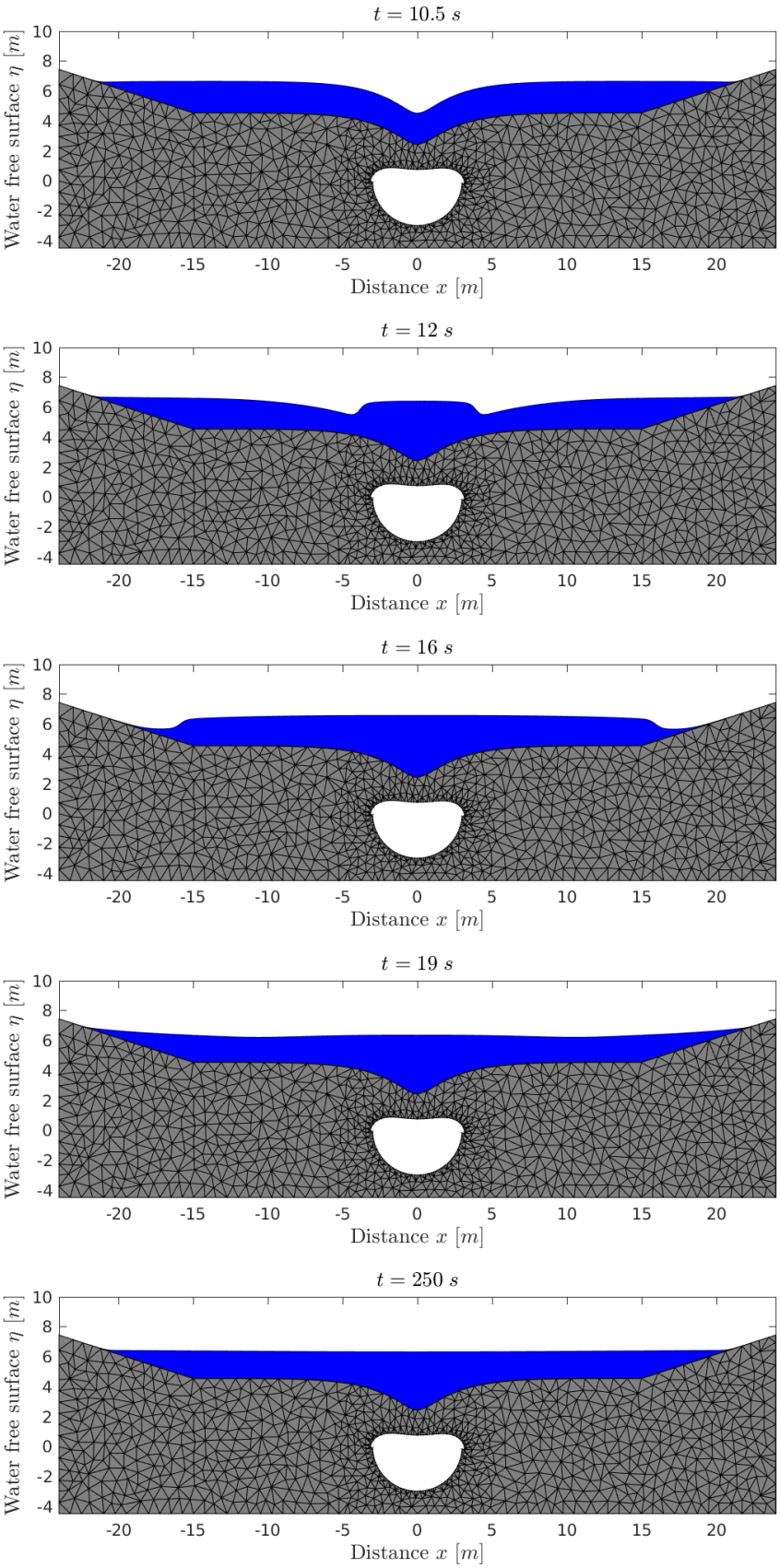

Figure 4.11: Free-surface responses at five different instants obtained for the flow problem over a deformable bed with $\beta = \frac{\pi}{10}$.

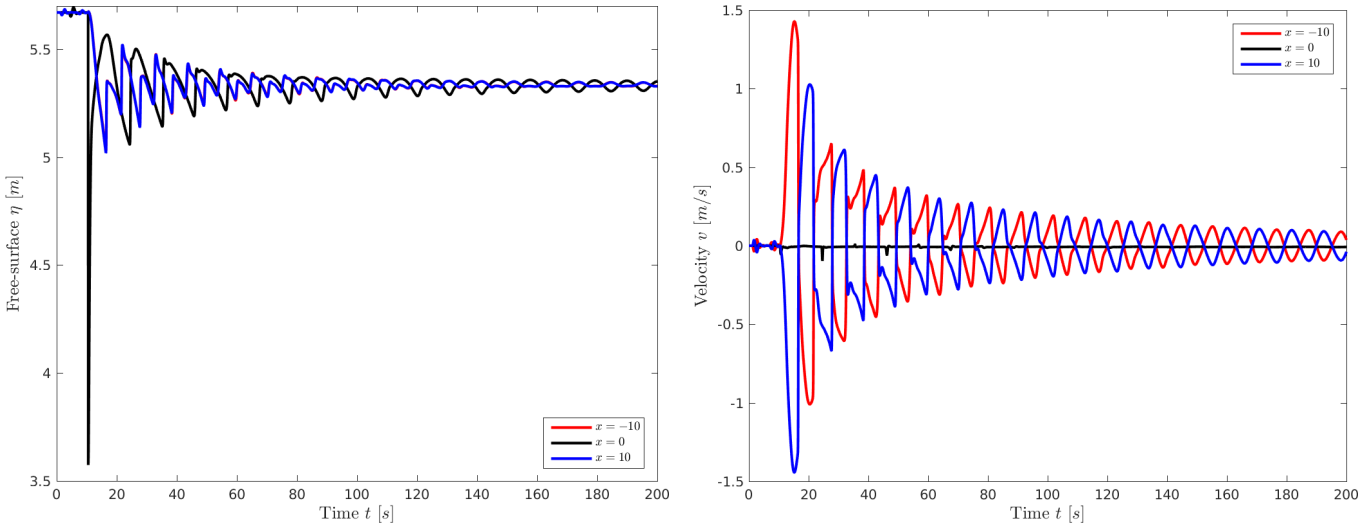

Figure 4.12: Time evolution of the water free-surface (left) and flow velocity (right) at three different gauges for the flow problem over a deformable bed with $\beta = \frac{\pi}{5}$.

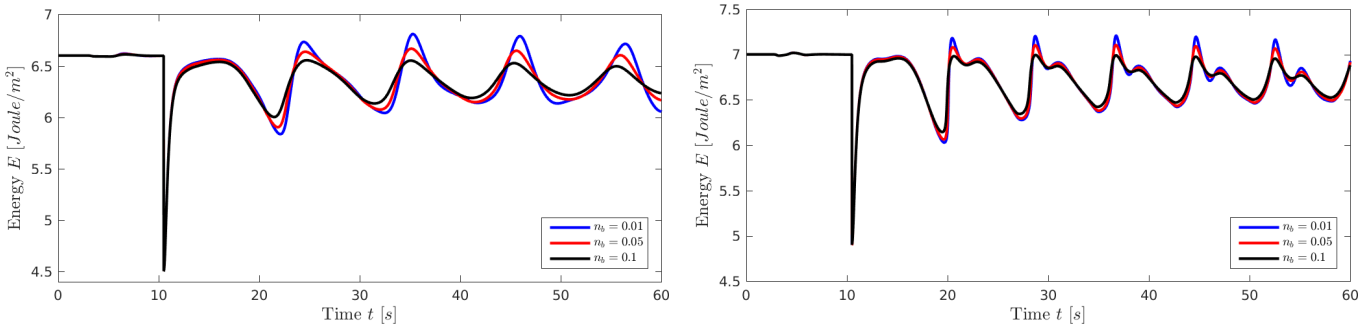

Figure 4.13: Time evolution of the hydraulic energy for free-surface flow problem over a deformable bed using different Manning coefficients with $\beta = \frac{\pi}{5}$ (left) and $\beta = \frac{\pi}{10}$ (right).

order to quantify these results, we summarize in Table 4.1 statistics on the results shown for the hydraulic energy in Figure 4.13. Here, we present the minimum value, peak value, mean value, standard deviation, rise and settling times obtained for the considered Manning coefficients. The effect of bed frictions related to the Manning roughness can be clearly seen on the rise and settling times. Same conclusions have been exhibited for similar quantitative results for the situation with $\beta = \frac{\pi}{10}$. Again, the proposed hybrid finite volume/finite element method performs very satisfactorily for this flow problem since it does not diffuse the moving bed fronts and no spurious oscillations have been detected near steep gradients of the runup waves in the computational domain. In addition, the wet/dry treatment considered in this study resolves well the runup waves.

5 Conclusions

In the present work, we have used a coupled system of nonlinear shallow water equations and linear elasticity to model and simulate wave runup by a deformation on seabeds. In order to reduce the complexity of the problem we have considered a static approximation of the bed deformation. The system is fully coupled through transfer conditions at the interface between the water flow and the seabed. In the current study, hydrostatic pressure and friction forces are considered for the elastostatic equations whereas bathymetric forces are accounted for in the shallow water equations. A hybrid finite volume/finite element is considered for the numerical simulation and a special wet/dry treatment is accounted for in our approach. The method is well-balanced, stable and it accurately resolves both water free-surface and bed deformations. The proposed method has been applied to a dam-break problem over a non-flat dry bed. The obtained results for this free-surface flow problem using the finite volume method have shown good agreement with experimental measurements. We have also presented an application of the developed model for a free-surface flow problem over a deformable bed. The obtained results, even with a coarse mesh in complex geometry, indicate that the proposed model can be used as a robust tool to design wave runups by static deformation on seabeds. As future work, we aim to include erosion and deposition effects in the coupled model to allow for sediment transport and morphodynamics in the shallow water flows. Although, we have studied only the case of two-dimensional problems of the presented method, the extension to three-dimensional problems would be an encouraging next step and requires an in-depth study on free-surface problems to deal with the nonlinear structure of the wave runups. The future research should also be focused on the extension of these techniques to nonlinear plasticity in the bed deformation to allow strong interactions of water flows on soft beds.

Acknowledgment. The authors would like to thank anonymous referees for giving very helpful comments and suggestions that have greatly improved this paper.

References

[1] A. Al-Ghosoun, M. Herty, and M. Seaid. A new numerical treatment of moving wet/dry fronts in dam-break flows. *Journal of applied mathematics and computing*, 59:489–516, 2019.

[2] D. Alexander and P. Liu. Seepage force on a pipeline buried in a poroelastic seabed under wave loadings. *Applied ocean research*, 8:22–23, 1986.

[3] F. Benkhaldoun and M. Seaid. A simple finite volume method for the shallow water equations. *Journal of computational and applied mathematics*, 234:58–72, 2010.

[4] A. Bollermann, G. Chen, A. Kurganov, and S. Noelle. A well-balanced reconstruction of wet/dry fronts for the shallow water equations. *J Sci Comput*, 56:267–290, 2013.

[5] H. Çağatay and S. Kocaman. Experimental study of tailwater level effects on dam break flood wave propagation. In *Proceedings River Flow*, pages 635–644, 2008.

[6] C. Chen, C. Shen, C. Chen, and M. Cheng. Stability analysis of an oceanic structure using the Lyapunov method. *Engineering Computations*, 27:186–204, 2010.

[7] A. Ern, S. Piperno, and K. Djade. A well-balanced Runge-Kutta discontinuous Galerkin method for the shallow water equations with flooding and drying. *Int. J. Numer. Methods Fluids*, 58:1–25, 2008.

[8] D. Fuhrman and P. Madsen. Tsunami generation, propagation, and run-up with a high order Boussinesq model. *Coastal Engineering*, 56:747–758, 2009.

[9] B. Gatmiri. A simplified finite element analysis of wave-induced effective stress and pore pressure in permeable sea beds. *Geotechnique*, 40:15–30, 1990.

[10] A. Al Ghosoun, M. Herty, and M. Seaid. A new numerical treatment of moving wet/dry fronts in dam-break flows. *Journal of Applied Mathematics and Computing*, 59:489–516, 2019.

[11] B. Ginting and R. Mundani. Comparison of shallow water solvers: Applications for dam-break and Tsunami cases with reordering strategy for efficient vectorization on modern hardware. *Water*, 11:1–31, 2019.

[12] S. Hargarten and J. Robl. Modeling rapid mass movements using the shallow water equations. *Natural hazards and earth system sciences*, 2:6775–6809, 2019.

[13] D. Jeng. Soil response in cross-anisotropic seabed due to standing waves. *J. Geotech. Geoenviron. Eng*, 123:9–19, 1997.

[14] G. Kesserwani and Q. Liang. Locally limited and fully conserved RKDG2 shallow water solutions with wetting and drying. *Journal of scientific computing*, 50:120–144, 2012.

[15] G. Kirstetter, J. Hu, O. Delestre, F. Darboux, P. Lagree, S. Popinet, J. Fullana, and C. Josserand. Modeling rain-driven overland flow empirical versus analytical friction terms in the shallow water approximation. *Journal of Hydrology*, 536:1–9, 2016.

[16] A. Koukouselis, K. Chatziioannou, E. Mistakidis, and V. Katsardi. Development of an equivalent static method for the approximation of the dynamic response of offshore structures. *Engineering Computations*, 36:1121–1141, 2019.

[17] A. Kreuzhuber, Z. Horvath, S. Noelle, G. Bloschi, and J. Waser. A fast second-order shallow water scheme on two-dimensional structured grids over abrupt topography. *Advances in water resources*, 127:89–108, 2019.

[18] Q. Liang and F. Marche. Numerical resolution of well-balanced shallow water equations with complex source terms. *Advances in water resources*, 32:873–884, 2009.

[19] M. Luan, P. Qu, D. Jeng, Y. Guo, and Q.Yang. Dynamic response of a porous seabed-pipeline interaction under wave loading: Soil-pipeline contact effects and inertial effects. *Computers and geotechnics*, 35:173–186, 2008.

[20] W. Magda. Wave-induced uplift force on a submarine pipeline buried in a compressible seabed. *Ocean engineering*, 24:551–576, 1997.

[21] S. Okusa. Measurements of wave-induced pore pressure in submarine sediments under various marine conditions. *Marine geotechnology*, 6:119–144, 1985.

[22] S. Okusa and A. Uchilda. Pore-water pressure change in submarine sediments due to waves. *Marine geotechnology*, 4:145–160, 1980.

[23] E. Playan, R. Walker, and P. Merkley. Two-dimensional simulation of basin irrigation I: Theory. *J. Irrig. Drainage*, 31:837–855, 1994.

[24] H. Poulos and E. Davis. *Elastic solutions for soil and rock mechanics*. The University of Sydney, Australia, 1991.

[25] S. Pudjaprasetya and A. Ribal. Numerical solution of Saint Venant equation to study floods in rivers. *Coastal Engineering*, 56:747–758, 2009.

[26] K. Ramadan, H. Hassan, and S. Hanna. Modeling of tsunami generation and propagation by a spreading curvilinear seismic faulting in linearized shallow-water wave theory. *Applied mathematical modelling*, 35:61–79, 2011.

[27] P. Roe. Approximate Riemann solvers, parameter vectors, and different schemes. *Journal of computational physics*, 43:357–372, 1981.

[28] A. Sielecki and G. Wurtele. The numerical integration of the nonlinear shallow water equations with sloping boundaries. *J. Phys*, 6:219–236, 1970.

[29] G. Strang. On the construction and the comparison of difference schemes. *SIAM J. Numer. Anal.*, 5:506–517, 1968.

[30] Y. Sun, S. Chen, and Y. Yang. The families of nonconforming mixed finite elements for linear elasticity on simplex grids. *Applied mathematics and computation*, 358:348–362, 2019.

[31] R. Touma. Well-balanced central schemes for systems of shallow water equations with wet and dry states. *Applied mathematical modelling*, 5:1–17, 2015.

[32] Y. Tsui and C. Helfrich. Wave-induced pore pressure in submerged sand layer. *Journal of geotechnical engineering*, 109:603–618, 1983.

[33] G. Wang, Y. Zhang, and T. Nogami. Wave-induced seabed response analysis by radial point interpolation meshless method. *Ocean engineering*, 31:21–42, 2004.

[34] Y. Ying and Y. Wang. Improved implementation of the HLL approximate Riemann solver for one dimensional open channel flows. *Journal of Hydraulic Research*, 46:21–34, 2008.

[35] K. Zen and H. Yamazaki. Field observation and analysis of wave-induced liquefaction in seabed. *Soils and foundations*, 31:161–179, 1991.

[36] H. Zhang, M. Zhang, Y. Ji, Y. Wang, and T. Xu. Numerical study of tsunami wave run-up and land inundation on coastal vegetated beaches. *Computers & Geosciences*, 132:9–22, 2019.

[37] M. Zhang and W. Wu. A two dimensional hydrodynamic and sediment transport model for dam break based on finite volume method with quadtree grid. *Applied Ocean Research*, 33:297–308, 2011.

[38] X. Zhang, C. Xu, and Y. Han. Three-dimensional poro-elasto-plastic model for wave-induced seabed response around submarine pipeline. *Soil dynamics and earthquake engineering*, 69:163–171, 2015.